




Si₃N₄ nanofelts/paraffin composites as novel thermal energy storage architecture

Francesco Valentini^{1,*} , Andrea Dorigato¹, Alessandro Pegoretti¹, Michele Tomasi¹, Gian D. Sorarù¹, and Mattia Biesuz¹

¹Department of Industrial Engineering and INSTM Research Unit, University of Trento, Via Sommarive 9, 38123 Trento, Italy

Received: 21 April 2020

Accepted: 31 August 2020

Published online:

14 September 2020

© The Author(s) 2020

ABSTRACT

The environmental problems associated with global warming are urging the development of novel systems to manage and reduce the energy consumption. An attractive route to improve the energy efficiency of civil buildings is to store the thermal energy thanks, during heating, to the phase transition of a phase-change material (as paraffin) from the solid to the liquid state and vice versa. The stored energy can be then released under cooling. Herein, we developed a novel material (nanofelt) constituted by Si₃N₄ nanobelts able to absorb huge amounts of liquid paraffin in the molten state and to act as an efficient shape stabilizer. The nanofelt manufacturing technology is very simple and easy to be scaled-up. The effect of the Si₃N₄ nanofelts density and microstructure on the paraffin sorption and leakage and on the thermal properties of the resulting composite structures is investigated. It is shown that the produced Si₃N₄/-paraffin composites are able to retain enormous fractions of paraffin (up to 70 wt%) after 44 day of desorption test on absorbent paper towel. The thermal energy storage efficiency measured through calorimetric tests is as high as 77.4% in heating and 80.1% in cooling.

Introduction

In the last decades, the accumulation of greenhouse gases related to human activities has caused chemical changes in the atmosphere, becoming the main reason for global warming [1–3]. In this context, the development of energy storage systems is essential for managing the energy demand and for reducing

the human carbon footprint. Such systems work as accumulators of an available energy form (thermal, electric, chemical, etc.) which can be used at a later time [3–7]. Thermal energy storage (TES) allows the accumulation of thermal energy that can be used for thermal management applications, such as to balance the energy demand of civil buildings, thus reducing the energy absorption peaks [7–10]. Among the different TES architectures, latent heat thermal energy

Handling Editor: N. Ravishankar.

Address correspondence to E-mail: francesco.valentini@unitn.it

<https://doi.org/10.1007/s10853-020-05247-5>

storage systems are of great interest as they allow to store huge amounts of thermal energy (at a constant temperature) thanks to the phase transition of a material from a physical state to another (for example from liquid to solid and vice versa) [10–13]. For this reason, they are mostly based on the so-called phase-change materials (PCM). Paraffins are the most used organic-PCM due to the low cost, the high heat of fusion/solidification, the broad range of melting temperatures and the chemical stability [13, 14]. They are mainly used for the production of thermoregulated building materials [15–18], solar energy storage devices [19], sport equipment [20, 21], multifunctional composites [22, 23] and smart fabrics [24–27]. The recent European requirements concerning the achievement of nearly zero-energy buildings (NZEBs) [28] represent a new stimulus for the research of novel thermally insulating materials and thermal energy storage systems.

The main drawback related to the use of paraffin-based PCMs is their leakage in the molten state, which requires the confinement of the PCM either by encapsulation [26, 29] or by shape stabilization [30–32]. Shape stabilization can be performed using polymer matrices, such as high-density polyethylene [33], polypropylene [34], poly(methyl methacrylate) [35], polyurethane copolymers [36], acrylic resins [37] and styrene-butadiene-styrene rubber [38]. Moreover, in the last few years also porous ceramics (such as expanded graphite, iron ore tailings, silica, etc.) have been considered for the shape stabilization of paraffins [39–41].

The recent developments in the field of polymer-derived ceramics (PDC) [42] have allowed the production of new porous ceramic structures [43] as aerogels [44], cellular structures [45], foams [46, 47], 3D-printed architectures [48–51], mesoporous structures [52, 53] and fibrous ceramics [54]. PDC technology is based on the pyrolysis of a pre-ceramic resin (polysiloxane, polycarbosilane, polysilazane, etc.) in controlled atmosphere. At high temperature the resin loses its organic part leaving a ceramic structure whose composition depends both on the resin chemistry and on the pyrolysis atmosphere.

In a recent patent [55], we have disclosed a novel polymer-derived-ceramic (PDC) synthesis route for the preparation of α - Si_3N_4 nanofibrous structures (nanofelts). The process is pretty simple and allows the production of nanofelts with various geometries of possible industrial interest [56, 57]: an open-cells

polyurethane foam is impregnated with a polysiloxane and pyrolyzed in N_2 . At low temperature ($< 1000\text{ }^\circ\text{C}$) the pre-ceramic resin is converted into an amorphous SiOC network embedding nano-graphitic carbon clusters [58, 59]; this structure replicates the parent PU foam geometry. At about $1500\text{ }^\circ\text{C}$ the carbothermal reduction of silica begins releasing CO and SiO gasses. Then, SiO reacts with N_2 (from the atmosphere) within the SiOC foam cells, forming α - Si_3N_4 nanobelts. At the end of the process the SiOC is completely consumed leaving nanofibrous ceramic felts. Considering that (1) the nanofelts are characterized by extremely low density (open porosity ≈ 95 – 99.7%), (2) the Si–N bond is rather covalent ($\Delta\chi = 1.14$, corresponding to 27.7% ionic character, χ being the electronegativity) and (3) and single crystal silicon nitride has a high intrinsic thermal conductivity over $200\text{ W m}^{-1}\text{ K}^{-1}$ [60], these materials could represent a novel architecture for shape stabilization of apolar compounds (as paraffin).

On the basis of the considerations, the aim of the present work is to answer the following questions:

1. Can Si_3N_4 nanofelts act as an efficient shape stabilizer for paraffin-based TES applications?
2. Which are the thermal properties and the energetic performances of the resulting paraffin/ Si_3N_4 composites?

Experimental procedures

Different Si_3N_4 nanofelts were prepared following the procedure detailed in [55]. Open-cells polyurethane (PU) foams (A.R.E., Milan, Italy) with different cell size were employed; i.e. 30 and 90 pore per inch (PPI30 and PPI90, respectively). The foams were cut into rectangular samples with size about $30 \times 15 \times 3\text{ mm}^3$. These were impregnated with a liquid siloxane (SPR-036, Starfire, NY, USA) in acetone solution (SPR-036/PU = 2:1 weight ratio) and cross-linked with a Pt Karstedt's catalyst (CAS#: 68478-92-2; Sigma-Aldrich, Saint Louis, MO, USA,) diluted in xylene to 0.1% (50 μL of Pt catalyst per gram of SPR-036). The PU foams were impregnated with different amounts of pre-ceramic resin, the SPR-36: PU weight ratio ranging between 3:1 and 8:1 (this allowed to obtain felts with different densities). After 10 h drying at room temperature, the foams were pyrolyzed in a tubular alumina furnace (Lindberg/

Blue, USA) in N₂ atmosphere (300 cm³ min⁻¹). The pyrolysis was carried out at 1565 °C for 3 h (heating and cooling rate = 10 °C min⁻¹). A summary of the sample's names and of their characteristics in terms of processing parameters, density and porosity is reported in Table 1.

The microstructure of the nanofelts were analysed using a Zeiss Supra 40 field emission scanning electron microscope (FESEM) after metalization with a Pt-Pd sputtering. The mineralogical analysis was carried out by X-ray diffraction using a D/Max-B diffractometer (Rigaku Co, Tokyo, Japan), operating at 40 kV and 30 mA (CuKα radiation, 0.05° step, 4 s step⁻¹).

The nanofelts were used to absorb a Rubitherm RT21HC paraffinic wax (Rubitherm GmbH, Berlin, Germany), with a melting point of 21 °C and a melting enthalpy (ΔH_m) of 139 J g⁻¹. This PCM was selected to store/release thermal energy in a temperature interval near room temperature (civil building applications). The paraffin absorption was carried out on a heated plate at 40 °C and occurred within few minutes.

The ability of the materials to retain paraffin has been investigated through a leaking test performed in an oven at 40 °C. The specimens, after the production, were placed in the oven on an absorbent paper towel, and the mass of the specimens was monitored for a period of 44 days in order to determine the maximum quantity of paraffin that they are able to retain in the long period.

The Fourier transformed infrared spectra (FTIR) were acquired in attenuated total reflectance (ATR) mode using a Perkin Elmer FT-IR Spectrometer (Perkin-Elmer, Waltham, MA, USA); the working parameters were wavenumber range 4000–650 cm⁻¹, four scans, resolution of 4 cm⁻¹.

Thermogravimetric analysis (TGA) was performed on the prepared samples (after 14 days of desorption

on sorbent paper towel) through a TGAQ5000 thermobalance under an air flow (10 mL min⁻¹) from 30 to 700 °C (heating rate = 10 °C min⁻¹). The temperature associated to a mass loss of 5% (T_{5%}) and the temperature associated to the maximum rate of degradation (T_{peak}) and the residual mass at 700 °C (m₇₀₀) were determined. Differential scanning calorimetry (DSC) measurements were performed on the prepared samples (after 14 days of desorption on sorbent paper towel) using a Mettler DSC30 calorimeter under a nitrogen flow (10 cm³ min⁻¹). A heating scan from -30 to 50 °C was followed by a cooling stage from 50 to -30 °C. All the thermal ramps were carried out at 10 °C min⁻¹. In this way, the melting and crystallization temperature (T_m, T_c) and the specific melting and crystallization enthalpy values (ΔH_m, ΔH_c) were obtained. The volumetric specific enthalpy P was evaluated by multiplying the experimental enthalpy values by density, the density of each sample (ρ) was evaluated knowing the paraffin content and the density of the nanofelt matrix for heating and cooling, i.e. as P_{Heat}=ΔH_m*ρ and P_{Cool}=ΔH_c*ρ, respectively. In the case of paraffin, the density values reported in technical data sheet have been used (0.88 g cm⁻³ at the solid state, 0.77 g cm⁻³ at the liquid state). Moreover, the thermal energy storage efficiency was determined both during the heating scan (η_m) and the cooling scan (η_c) as the ratio between the specific enthalpy of the samples and the corresponding specific enthalpy values of the neat paraffin, as shown in Eqs. (1, 2):

$$\eta_m = \left(\frac{\Delta H_m}{\Delta H_{mPCM}} \right) \cdot 100 \tag{1}$$

$$\eta_c = \left(\frac{\Delta H_c}{\Delta H_{cPCM}} \right) \cdot 100 \tag{2}$$

where ΔH_{mPCM} and ΔH_{cPCM} are, respectively, the specific enthalpy values associated to the melting and crystallization of the neat PCM. The thermal analyses

Table 1 List of the prepared Si₃N₄ nanofelts

Sample name	PPI	SPR-036/PU (weight ratio)	Density (g/cm ³)	Porosity (%)
PPI90_189 (kg m ⁻³)	90	8:1	0.189	94.1
PPI90_136 (kg m ⁻³)	90	6:1	0.136	95.7
PPI90_84 (kg m ⁻³)	90	4:1	0.084	97.4
PPI30_61 (kg m ⁻³)	30	6:1	0.061	98.1
PPI30_45 (kg m ⁻³)	30	3:1	0.045	98.6

The sample's name reports the PPI (pores per inch) of the parent PU foam and the density of the pyrolysed samples

(TGA and DSC) were carried out after keeping the samples for 14 days at 40 °C on an absorbent paper towel (paraffin leakage test).

The reliability of the materials in terms of melting/crystallization enthalpy upon heating and cooling cycles was tested performing 20 repeated heating/cooling cycles from – 30 °C up to 70 °C using a Mettler DSC30 calorimeter under a nitrogen flow (10 cm³ min⁻¹).

The overall thermal performance of the materials (after 14 days of desorption on sorbent paper towel) was investigated recording their surface temperature using an infrared thermal imaging camera FLIR E60 (emissivity = 0.86). The specimens were heated in an oven at 40 °C overnight and then inserted in a climate chamber at a temperature of 5 °C; the surface temperature was then monitored for 60 min. At the same way, the specimens were cooled in a climatic chamber at 5 °C overnight and then inserted in an oven at a temperature of 40 °C; the surface temperature was then monitored for 60 min. In the heating test the time required to reach a temperature of 40 °C (t_{40}) has been evaluated, in the cooling test the time required to reach a temperature of 5 °C (t_5) has been evaluated.

Results and discussion

The main morphological, microstructural and mineralogical features of the nanofelts are reported in Fig. 1a–e. The nanofelts obtained using PPI90 PU foams are well-homogeneous, and the parent sponge structure (i.e. pores and struts) cannot be recognised with the naked eye (Fig. 1a). Conversely, the materials obtained using large-cell PU foams (i.e. PPI30) show a more inhomogeneous morphology which partially replicates the struts and cells of the parent PU foam (Fig. 1a). The phase analysis by XRD evidence that the main crystalline component of the nanofelt is α -Si₃N₄, with negligible amounts of its β polymorph (Fig. 1e). The felt microstructure is constituted by silicon nitride nanobelts, whose size primarily depend on the PU foam PPI: large cell-foams leading to thinner and longer Si₃N₄ fibres (Fig. 1c, d) [57]. The nanobelts are constituted by dense single crystals as shown by the TEM investigations reported in our previous work [57]. The transformation of the amorphous SiOC network into Si₃N₄ is complete (or almost complete) in all the samples with the

exception of the PPI90_189 kg m⁻³, where large amounts of relicts of SiOC struts are present in the pyrolysed component (Fig. 1b). This might be attributed to the fact that in this sample a large amount of pre-ceramic resin was used (Table 1), thus requiring the diffusion of more N₂ inside the felt to complete the reaction. It is also worth mentioning that the high fibre density in PPI90_189 kg m⁻³ reasonably hinders the N₂ diffusion and consequently retards the transformation.

The ability of the nanofelts to retain paraffin was evaluated through a leaking test; the results, in terms of m_f/m_0 , (where m_0 is the initial mass of the specimen and m_f the mass at the time of the measurement) in terms of wt% paraffin content and in terms of vol% paraffin content are reported in Fig. 2a–c, respectively.

Figure 2a reports that PPI30 samples show the highest mass increase due to paraffin absorption (m_f/m_0 value higher than 900%). This can be attributed to the fact that PPI30 samples are significantly less dense than the PPI90 ones, with open porosity exceeding 98% of the total volume (Table 1). However, PPI30 samples exhibit also the largest leakage; thus, at the end of the test these samples show the lowest m_f/m_0 ratio. Conversely, the samples PPI90_189 kg m⁻³, PPI90_136 kg m⁻³ and PPI90_84 kg m⁻³ are characterized by a lower weight gain due to paraffin absorption. The m_f/m_0 ratio scales with the starting density of the felt, denser felts being characterized by lower weight gain. However, PPI90 materials are characterized by a limited paraffin leakage, mostly concentrated in the first 10/15 days (the leakage is limited in particular for PPI90_136 kg m⁻³ and PPI90_84 kg m⁻³ samples). The differences in terms of leakage performance between PPI90 and PPI30 samples might be primarily attributed to the different morphology: PPI30 felts being characterized by a more inhomogeneous microstructure, which partially replicates the struts/pore of the parent PU foam (i.e. the reminiscence of parent PU foam structure can be clearly seen in Fig. 2a in case of PPI30 sample, while it is not detectable with the naked eye in case of PPI90 sample). The presence of regions with very low local density of fibres could represent preferential leakage paths.

From the results reported in Fig. 2b, it is possible to observe that all the samples are able to absorb a huge amount of paraffin (up to 90 wt% in the case of PPI30_45 kg m⁻³). Moreover, the samples PPI90_84

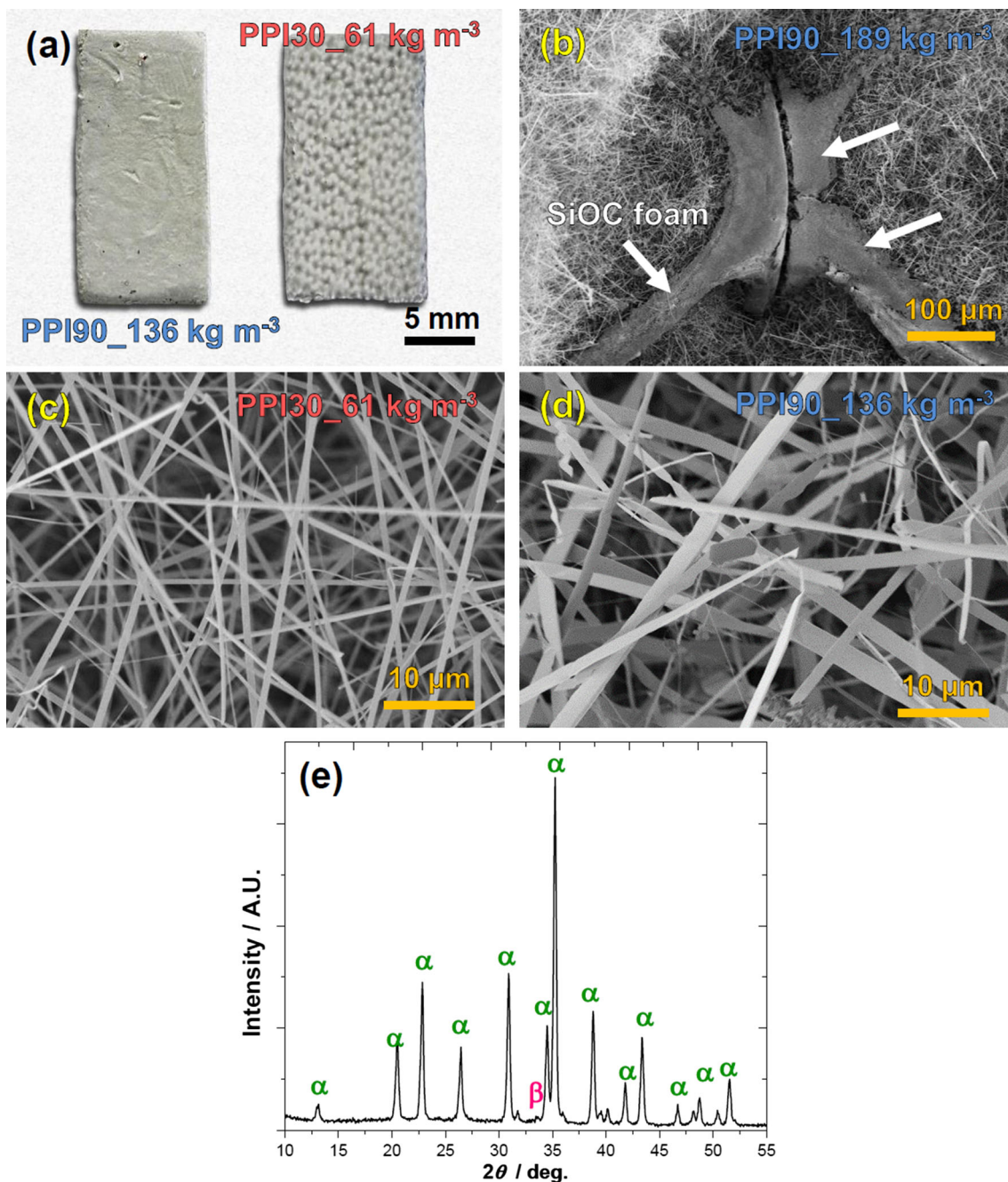


Figure 1 Digital camera picture of two selected PPI90 and PPI30 samples (a), SEM micrographs of the nanofelts (b–d) and XRD spectrum of the PPI_136 kg m⁻³ (e).

kg m⁻³ and PPI90_136 kg m⁻³ are able to retain paraffin with a very limited leakage (Table S1). The paraffin content is around 80 wt% after 14 days and around 75 wt% after 44 days (Table S2). All the other samples are characterized by a strong paraffin leakage (concentrated in the first 10 days) leading to a paraffin content of only ca 50 wt% and ca 25 wt% after 14 and 44 days, respectively. It is also possible to

observe that the paraffin-retaining ability of the nanofelts slightly increases with their density (i.e. comparing PPI30_45 kg m⁻³ and PPI30_61 kg m⁻³ samples or comparing PPI90_84 kg m⁻³ and PPI90_136 kg m⁻³ felts). This can be attributed to the fact that the number of fibres per unit of volume increases with the density of the felt, thus increasing the capillarity forces contrasting the the leakage. An

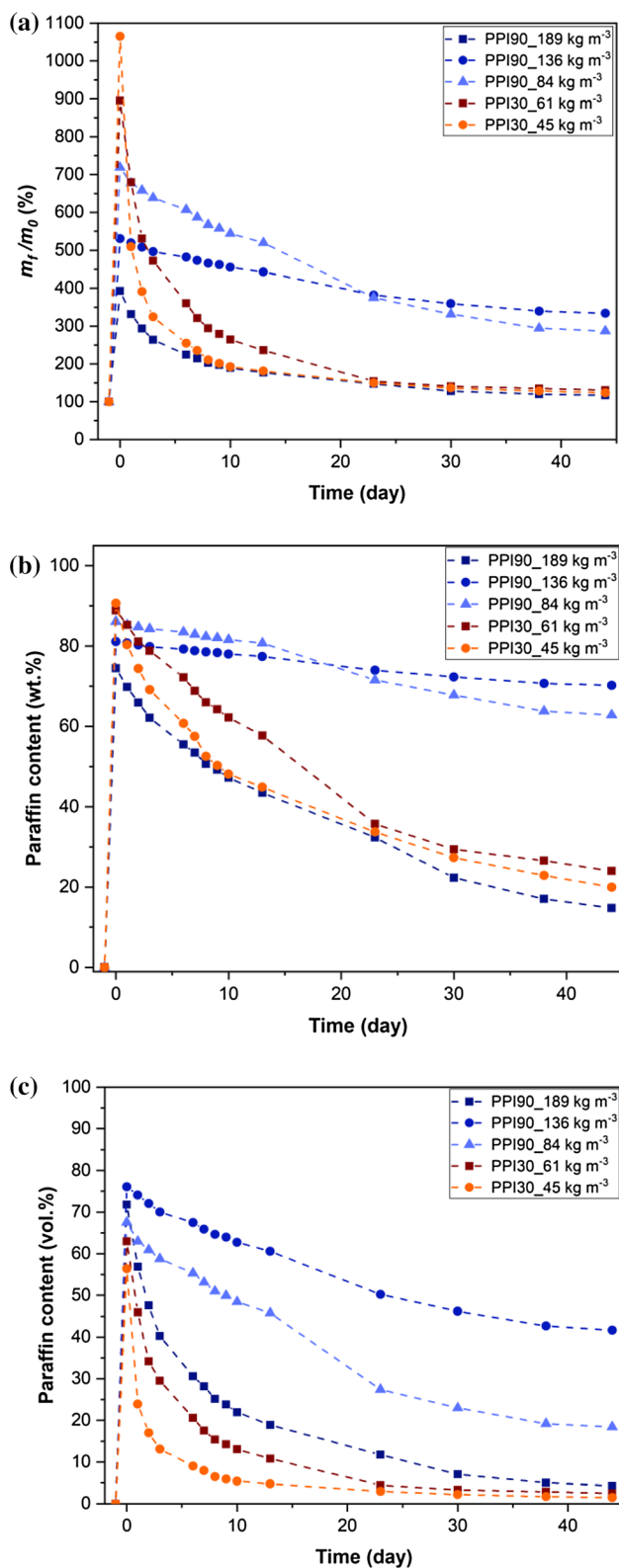


Figure 2 Desorption curves of the prepared samples in terms of **a** m_t/m_0 , **b** paraffin content wt.% and **c** paraffin content vol.%.

exception is represented by the PPI90_189 kg m⁻³ felt. Its different behaviour can be explained considering that it contains significant amounts of unreacted SiOC (Fig. 2b) that might represent preferential leakage regions.

From the results reported in Fig. 2c it is possible to observe that PPI90 samples are able to absorb up to 75 vol%, and the sample PPI90_136 kg m⁻³ is able to retain paraffin more than the other samples, with a paraffin content equal to 41.6 vol% after 44 days (Table S3). The samples PPI90_189 kg m⁻³ and PPI90_84 kg m⁻³ show a similar absorption capability but a release profile more rapid, similar to that of PPI30 samples that are able to retain only a very limited paraffin quantity (around 1–2 vol%).

The advantage of the Si₃N₄ matrix for the absorption of paraffin respect to common systems such as graphene foams and graphene oxide/carbon nanotubes composites is the short time required for the paraffin absorption: the Si₃N₄ matrix is able to absorb paraffin within few minutes, while in the case of graphene oxide 2 h of stirring at 90 °C is required, and in the case of graphene oxide and graphene oxide foam several hours of vacuum impregnation [61–63].

To confirm the hypothesis of no chemical reaction between the Si₃N₄ matrix and paraffin, FTIR measurements were performed. The FTIR spectra of PPI90_136 kg m⁻³ sample with and without paraffin and of neat paraffin are reported in Fig. 3.

Looking at the spectra of the PPI90_136 kg m⁻³ sample without paraffin, it is possible to observe a broad band in the range 800–1000 cm⁻¹ that can be attributed to the Si–N–Si asymmetrical stretching vibration of α-Si₃N₄. The peak at 1098 cm⁻¹ can be related to the Si–O vibrations in unreacted SiO₂ relicts. The peak at 683 cm⁻¹ can be attributed to the Si–N stretching vibration [64–66]. Looking at the spectrum of neat paraffin it is possible to observe three peaks in the range 2800–3000 cm⁻¹ that can be attributed to the C–H stretching vibration of –CH₂ and –CH₃ groups, while the peaks at 1466 and 1378 cm⁻¹ can be attributed to the C–H asymmetric and symmetric bending of –CH₂ and –CH₃ groups, respectively. The peak at 720 cm⁻¹ can be assigned to the CH₂ rocking vibration [29]. The curve of the PPI90_136 kg m⁻³ sample with paraffin presents both the absorption peaks of paraffin and of the matrix; in particular, no change in shape nor shift of the absorption peaks can be detected. This confirms the

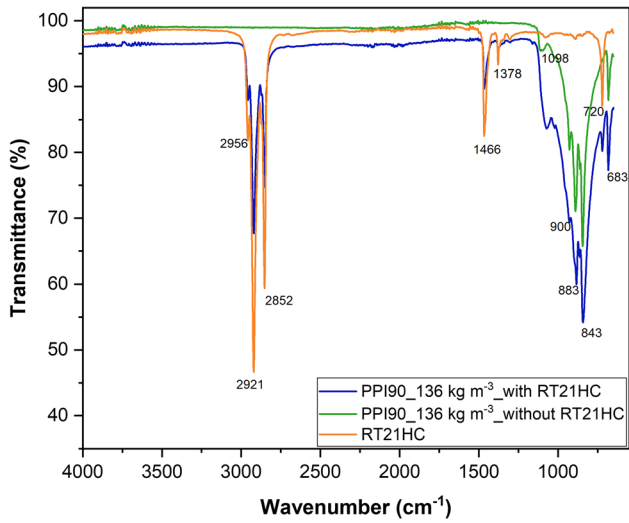


Figure 3 FTIR spectra of the PPI90_136 kg m⁻³ sample with and without paraffin and of neat paraffin (RT21HC). Spectra collected in ATR mode.

absence of chemical reactions between the matrix and paraffin due to the inert nature of the Si₃N₄ matrix.

The thermal behaviour of the samples after 14 days of leakage test on absorbent paper towel was investigated by TGA and DSC. The thermogravimetric curves of the PCM-impregnated nanofelts and of the neat PCM, are presented in Fig. 4 along with the corresponding derivative curves. The most representative results obtained from these tests are summarized in Table 2.

From the thermogram of the neat PCM sample it is evident that the degradation takes places in a single step at about 180 °C (corresponding to T_{peak}). The same behaviour can be observed for all the PCM-impregnated nanofelts, meaning that, as expected, no degradation of the ceramic structure occurs in this temperature range. The refractory properties of the ceramic structure might represent an advantage of this material in terms of safety (fire-proof) compared with other porous structure as expanded graphite or polymers which might burn or decompose when heated. The weight loss in our samples is only due to the degradation of the PCM. Looking at the values of $T_{5\%}$ is possible to observe that the paraffin incorporation in the nanofelt matrix increases the thermal stability of the materials, delaying the weight loss due to paraffin degradation of around 10 °C. Looking at the values of T_{peak} , it is possible to observe that, in case of samples containing a lower paraffin amount (PPI90_189 kg m⁻³, PPI30_61 kg m⁻³, PPI30_45 kg m⁻³) this temperature tends to be lower respect to

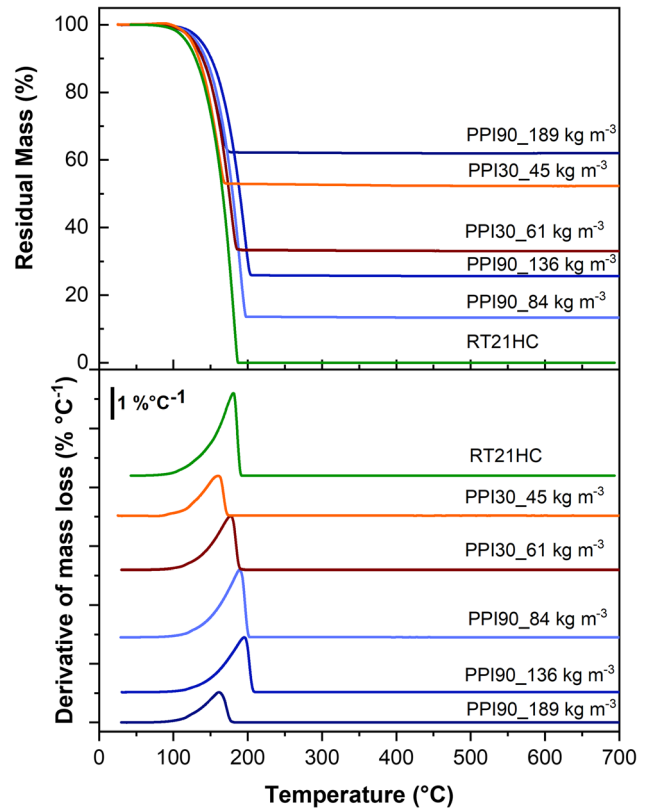


Figure 4 TGA curves of neat paraffin (RT21HC) and of the Si₃N₄/paraffin composites (after 14 days of desorption on sorbent paper towel).

Table 2 Results of the TGA test on neat paraffin (RT21HC) and on the Si₃N₄/paraffin composites (after 14 days of desorption on sorbent paper towel)

Sample	$T_{5\%}$ (°C)	T_{peak} (°C)	m_{700} (%)
RT21HC	117.8	180.7	0
PPI90_189 (kg m ⁻³)	126.9	161.1	62.0
PPI90_136 (kg m ⁻³)	137.5	195.3	25.7
PPI90_84 (kg m ⁻³)	131.4	188.9	13.4
PPI30_61 (kg m ⁻³)	127.5	177.0	33.1
PPI30_45 (kg m ⁻³)	124.6	160.7	52.3

that of paraffin; this effect can be due to the fact that paraffin is concentrated on the Si₃N₄ fibres (that have good thermal conductivity), and therefore the degradation is faster.

In case of samples containing higher paraffin amount (PPI90_84 kg m⁻³, PPI90_136 kg m⁻³), the decomposition temperature is slightly higher; in this case the heat is not enough to decompose the huge amount of paraffin, therefore heat has to pass

through the structure (that is characterized by the presence of voids) and the degradation process takes longer time. Looking at the residue at 700 °C (m_{700}), neat paraffin sample completely degrades, while for the other samples the soil residue is between 13 and 62% and corresponds to the mass of the nanofelt matrix. Moreover, comparing the values of paraffin content that can be estimated from the values of m_{700} , with the values of paraffin content after 13 days measured with the leaking tests and previously reported in Fig. 3b. It is possible to observe that these values are very similar; small differences can be noticed only in the case of PPI30_61 kg m⁻³ and in the case of PPI30_45 kg m⁻³. This is due to the fact that small variations of paraffin load within the same specimen could be expected, especially in case of PPI30 samples which shows a non-homogeneous morphology (Fig. 2a).

Remarkably, we can observe that the Si₃N₄ skeleton does not show any degradation upon heating, no thermal effects being visible above 250 °C. Si₃N₄ is in fact well-stable in inert atmosphere up to 1800 °C and in air up to 1100 °C [57]. This means that the structure is definitively more heat resistant and does not collapse at high temperature. It results therefore safer in case of fire, if it is compared with other organic [12, 18, 67] or carbon-based inorganic [61, 68] shape stabilizers.

In order to investigate the thermal properties of the materials, DSC tests were performed. The DSC thermograms collected in the first heating and in the cooling scan are presented in Fig. 5a, b, while the most important results obtained from these tests in the first heating and in the cooling scan are collected in Table 3.

From the thermograms it is possible to observe the melting peak of the PCM at about 20 °C, whose intensity is proportional to the paraffin content of each sample. A secondary melting peak of paraffin in the range -15–0 °C (about 11 J g⁻¹), is slightly detectable in the prepared samples. Moreover, it is worth noting that the shift of the T_m values in the samples PPI90_136 kg m⁻³ and PPI90_84 kg m⁻³ towards higher temperatures is probably a thermal effect due the presence of air inclusions in the material which reduces the thermal conductivity of the system. For the same reason, the T_c values of the PPI90_136 kg m⁻³ and PPI90_84 kg m⁻³ are lower (up to 10 degrees of difference) than those shown by the RT21HC sample. Usually when dealing with TES,

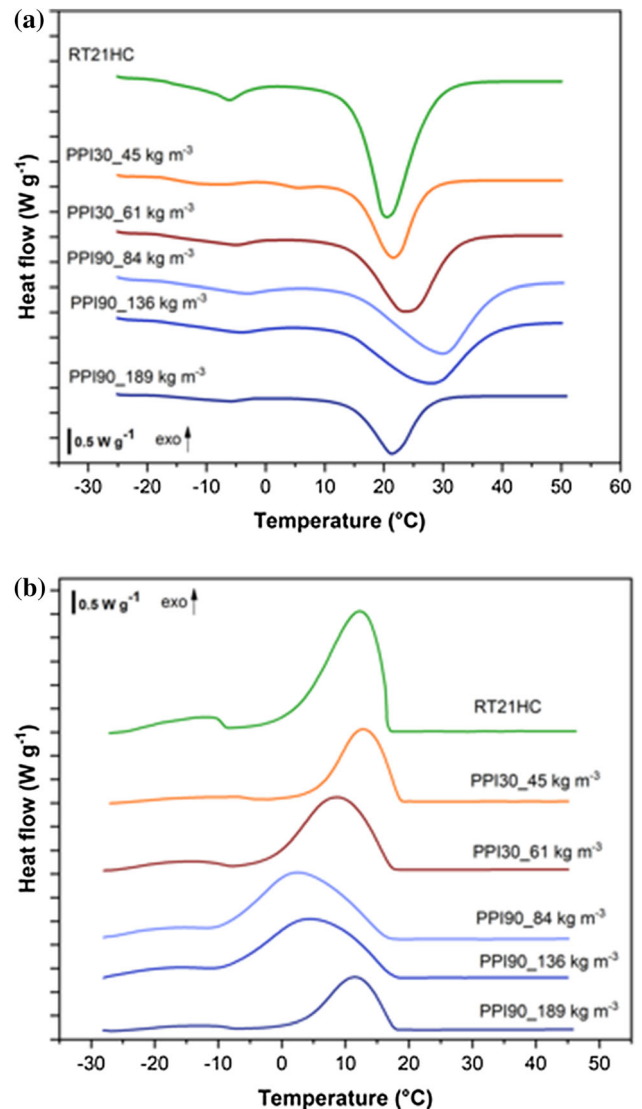


Figure 5 DSC curves of neat paraffin (RT21HC) and of the Si₃N₄/paraffin composites (after 14 days of desorption on sorbent paper towel): **a** heating scan, **b** cooling scan.

one would require very high thermal conductivity and reduced shift in the melting temperature with respect to the pure PCM [22, 27, 31]. While this is indeed true in high and medium temperature applications (solar towers, industrial furnaces, etc.), it might not be the case in low temperature systems, as thermal management of civil buildings. Here, the seasonal or night-day cycles are very slow, thus leaving enough time for the heat to diffuse inside the PCM/shape stabilizer composite (even if their thermal conductivity is modest). It might even be considered a positive effect, if the PCM latent heat is

Table 3 Results of the DSC tests on neat paraffin (RT21HC) and on the Si₃N₄/paraffin composites (after 14 days of desorption on sorbent paper towel)

Sample	T_m (°C)	ΔH_m (J g ⁻¹)	P_{heat} (J cm ⁻³)	η_m (%)	T_c (°C)	ΔH_c (J g ⁻¹)	P_{cool} (J cm ⁻³)	η_c (%)
RT21HC	19.4	139.1	107.1	100.0	12.3	149.7	131.7	100.0
PPI90_189 (kg m ⁻³)	21.4	58.0	25.6	41.7	11.5	60.8	29.8	40.6
PPI90_136 (kg m ⁻³)	28.2	107.7	67.5	77.4	4.7	111.3	79.2	74.3
PPI90_84 (kg m ⁻³)	29.9	102.2	65.2	73.5	2.3	119.9	87.2	80.1
PPI30_61 (kg m ⁻³)	24.1	101.3	47.6	72.8	8.7	108.4	57.8	72.4
PPI30_45 (kg m ⁻³)	21.6	68.9	25.5	49.5	12.9	77.1	32.3	51.5

slowly releases and absorbs the thermal energy for a few hours cycle.

Analysing ΔH_m and ΔH_c values, it emerges that the melting and crystallization enthalpy values are proportional to the paraffin amount. Moreover, the samples PPI90_136 kg m⁻³, PPI90_84 kg m⁻³ and PPI30_61 kg m⁻³ show interesting thermal energy storage capabilities, both in heating and in cooling. Comparing the η_m and the η_c with the results of the leaking test (reported in Fig. 3b) it is possible to observe that the values, in terms of paraffin content, in each sample are very similar. Small differences can be observed in case of PPI90_84 kg m⁻³ and PPI30_61 kg m⁻³ and can be due to an inhomogeneous distribution of the PCM within the samples. The volumetric thermal parameter of the PPI90_136 kg m⁻³ has been evaluated around 67 J cm⁻³ in heating (P_{Heat}) and around 80 J cm⁻³ in cooling (P_{Cool}): these values are very high and confirm the results obtained from the leaking test reported in Fig. 3c.

Comparing the three samples with higher thermal energy storage efficiency (PPI90_136 kg m⁻³, PPI90_84 kg m⁻³ and PPI30_61 kg m⁻³) it is possible to conclude that the PPI90_136 kg m⁻³ is the most promising material and the one with the lowest temperature difference respect to the melting and crystallization point of neat paraffin. The measured thermal energy storage efficiency was as high as 77.4% on heating and 80.1% on cooling. These values are comparable or larger to other results published in the scientific literature for other inorganic shape stabilizers [40, 61, 68]. But this new architecture possesses two fundamental advantages:

- (1) The synthesis route is very simple and flexible [57] compared with other inorganic skeletons [40] produced by sol-gel techniques (requiring a more sophisticated chemistry and reactant

control) followed by supercritical drying (very expensive and slow);

- (2) Si₃N₄ is fire resistant, inert and does not burn if heated or in case of fire (as would happen in carbon-based architectures [61, 68]).

The efficiency value obtained from the use of the PPI90_136 kg m⁻³ (around 77%) is much higher respect to the efficiency that can be obtained using graphene oxide as shape stabilizer for paraffin (around 50%) [61]. On the other hand the use of graphene foams and graphene oxide/carbon nanotubes composites results in enthalpy values that are around 99% [62, 63], but these compounds are not stable in temperature and thus can be considered dangerous in case of fire; moreover, vacuum impregnation is necessary in order to absorb paraffin.

In Fig. 6 the results of the thermal cycling test performed on the most promising sample (PPI90_136 kg m⁻³) are shown. It is possible to observe that the melting and crystallization enthalpies after 20 heating/cooling cycles are the same of the first cycle: this demonstrate the reliability of the composite material in this study.

Figures 7a, b and 8a, b show the thermal images of the samples during cooling and heating, respectively. Looking at the images acquired after 1 min from the beginning of the test (Figs. 7a, 8a), it is possible to observe that all the five specimens are visible, but the intensity of Sp1, Sp5, Sp6 is low; these points correspond to the samples PPI90_189 kg m⁻³, PPI30_61 kg m⁻³, PPI30_45 kg m⁻³ that have lower PCM content. Looking at Figs. 7b and 8b, acquired after 10 min from the beginning of the test, it is possible to observe that only the PPI90_136 kg m⁻³ and PPI90_84 kg m⁻³ are still visible, thanks to the higher PCM content.

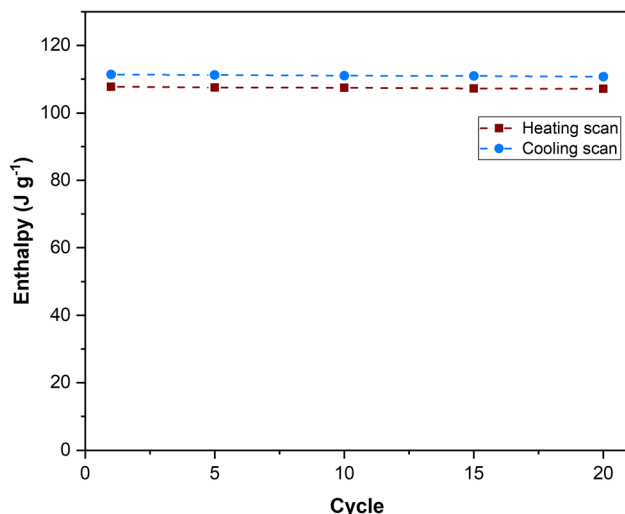


Figure 6 Results of the thermal cycling test performed on the PPI90_136 kg m⁻³ sample.

Figure 9a, b reports the result of the thermal imaging test. Both in the heating and in the cooling test the starting temperature is slightly different respect to the estimated one (5 °C in heating, 40 °C in cooling) due to the time required to move the samples from the oven to the climatic chamber and vice versa. In the cooling test (Fig. 9a), for the samples PPI90_136 kg m⁻³ and PPI90_84 kg m⁻³ the temperature decreases with a plateau-like trend due to the crystallization of the PCM. In the other samples this behaviour is only slightly detectable due to the lower PCM content. A very similar behaviour can be observed in the heating test (Fig. 9b): for the samples PPI90_136 kg m⁻³ and PPI90_84 kg m⁻³ the temperature increases with a plateau-like trend due to

the melting of the PCM, while in the other samples this behaviour is only slightly detectable due to the lower PCM content.

From the results of the thermal imaging, reported in Table 4 in terms of time needed to reach the final temperature, it is possible to observe that the time required to reach 40 °C is about 30 min for the samples PPI90_136 kg m⁻³ and PPI90_84 kg m⁻³, while it is only 11 min for the PPI30_45 kg m⁻³. Moreover, it is possible to observe that the time required to reach 5 °C are generally lower respect to the t_{40} . The reason for this behaviour is the difference of the thermal conductivity of paraffin between the liquid and the solid state [69]: at the solid state the thermal conductivity is higher, therefore during cooling the crystallization process is accelerated by fast heat diffusion through the solid. On the contrary, during heating, the melting process is hindered due to the lower thermal conductivity of the liquid paraffin formed on the samples surface, leading to a longer time to reach the final temperature.

Conclusions

Si₃N₄ nanofelts can act as a novel architecture for shape stabilization of paraffin-based PCM. The paraffin absorption and leakage strongly depend on the nanofelt density and on the choice of the parent polyurethane foam used to manufacture the nanofelts. The best results in terms of paraffin leakage and thermal performances are obtained when using small-cell polyurethane foams precursors (i.e. 90 pore

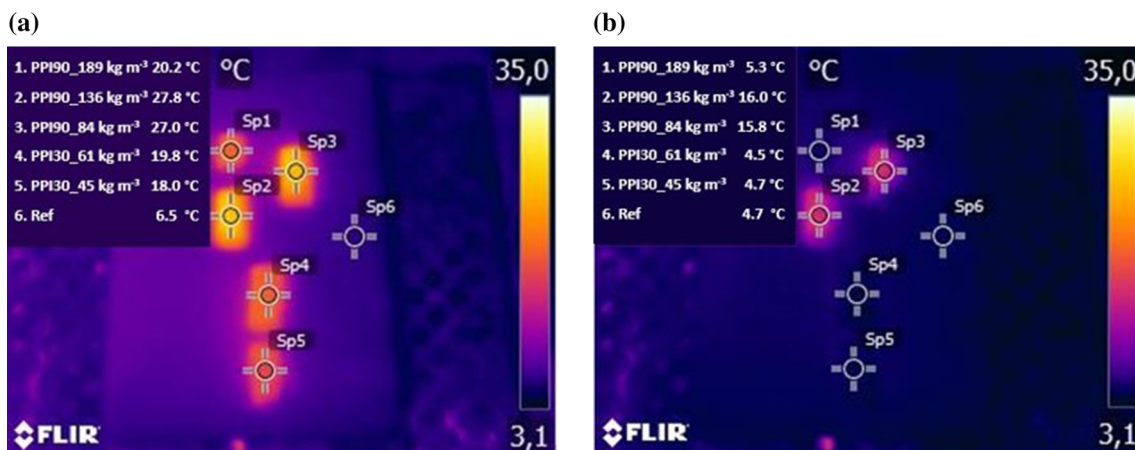


Figure 7 Thermal images of prepared samples and of the reference temperature of the climatic chamber (ref) the during cooling **a** after 1 min and **b** after 10 min (samples tested after 14 days of desorption on sorbent paper towel).

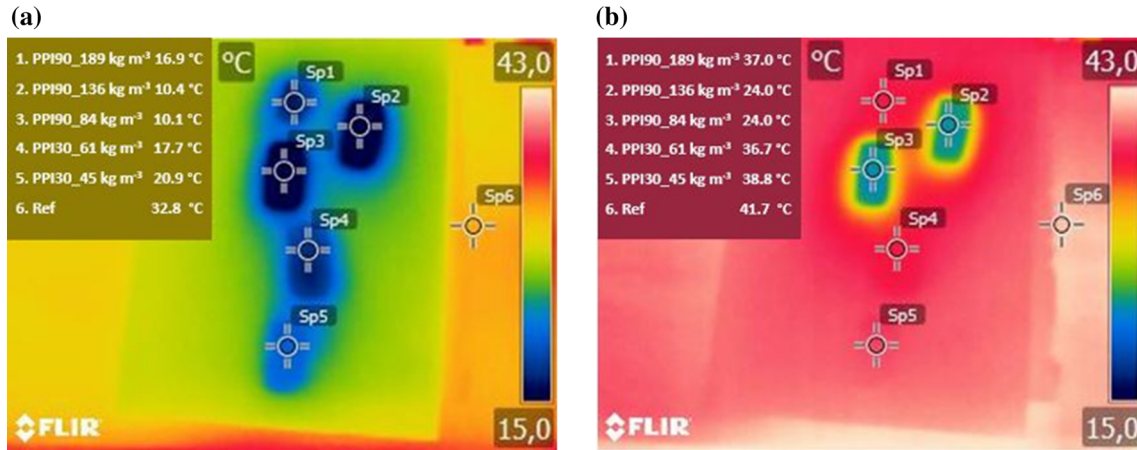


Figure 8 Thermal images of the prepared samples and of the reference temperature of the oven (ref) during heating **a** after 1 min and **b** after 10 min (samples tested after 14 days of desorption on sorbent paper towel).

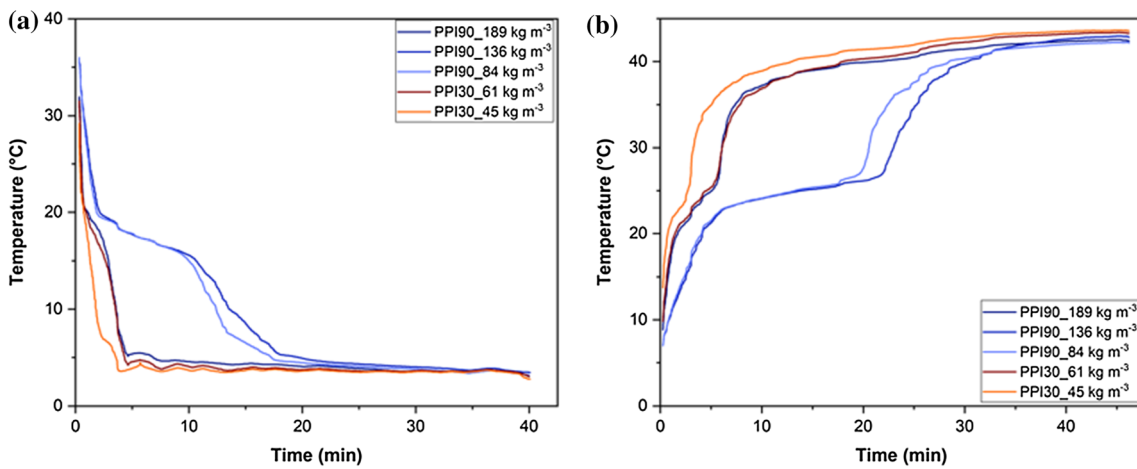


Figure 9 Temperature profiles of prepared samples: **a** cooling and **b** heating stage (samples tested after 14 days of desorption on sorbent paper towel).

Table 4 Results of the thermal imaging tests on the prepared nanofelts

Sample	t_5 (min)	t_{40} (min)
PPI90_189 (kg m^{-3})	5.1	18.0
PPI90_136 (kg m^{-3})	21.7	29.8
PPI90_84 (kg m^{-3})	18.5	28.4
PPI30_61 (kg m^{-3})	4.5	17.7
PPI30_45 (kg m^{-3})	3.8	11.7

per inch). In particular we have identified a composition (PPI90_136 kg m^{-3}) characterized by a minimal paraffin leakage and able to retain up to 70 wt% of paraffin after 44 days of desorption test. This composition is characterized by high thermal energy

storage efficiency (77%) and by a specific melting enthalpy higher than 100 J g^{-1} . Moreover, the thermal imaging test revealed that, thanks to phase transition of the PCM, the time needed to reach a specific temperature (40 °C) is three times higher in the case of the sample PPI90_136 kg m^{-3} respect to the PPI30_45 kg m^{-3} .

Acknowledgements

M. Biesuz and G. D. Sorarù kindly acknowledge the support from the Italian Ministry of University and Research (MIUR) within the programs PRIN2017 - 2017PMR932 “Nanostructured Porous Ceramics for Environmental and Energy Applications” and PRIN2017 - 2017FCFYHK “DIRECTBIOPOWER”.

Funding

Open access funding provided by Università degli Studi di Trento within the CRUI-CARE Agreement.

Compliance with ethical standards

Conflict of interest The authors declare that they have no conflict of interest.

Electronic supplementary material: The online version of this article (<https://doi.org/10.1007/s10853-020-05247-5>) contains supplementary material, which is available to authorized users.

Open Access This article is licensed under a Creative Commons Attribution 4.0 International License, which permits use, sharing, adaptation, distribution and reproduction in any medium or format, as long as you give appropriate credit to the original author(s) and the source, provide a link to the Creative Commons licence, and indicate if changes were made. The images or other third party material in this article are included in the article's Creative Commons licence, unless indicated otherwise in a credit line to the material. If material is not included in the article's Creative Commons licence and your intended use is not permitted by statutory regulation or exceeds the permitted use, you will need to obtain permission directly from the copyright holder. To view a copy of this licence, visit <http://creativecommons.org/licenses/by/4.0/>.

References

- [1] Alexiadis A (2007) A review of climate change, mitigation and adaptation. *Ecol Model* 203(3–4):243–256
- [2] Karakurt I, Aydin G, Aydiner K (2012) Sources and mitigation of methane emissions by sectors: a critical review. *Renew Energy* 39(1):40–48
- [3] Mofijur M et al (2019) Phase change materials (PCM) for solar energy usages and storage: an overview. *Energies* 12(3167):1–20
- [4] Anisur MR et al (2013) Curbing global warming with phase change materials for energy storage. *Renew Sustain Energy Rev* 18:23–30
- [5] Fernandes D et al (2012) Thermal energy storage: “How previous findings determine current research priorities”. *Energy* 39(1):246–257
- [6] Kant K, Shukla A, Sharma A (2017) Advancement in phase change materials for thermal energy storage applications. *Sol Energy Mater Sol Cells* 172:82–92
- [7] Li G, Zheng X (2016) Thermal energy storage system integration forms for a sustainable future. *Renew Sustain Energy Rev* 62:736–757
- [8] Meshgin P, Xi Y, Li Y (2012) Utilization of phase change materials and rubber particles to improve thermal and mechanical properties of mortar. *Constr Build Mater* 28(1):713–721
- [9] Bo H, Martin V, Setterwall F (2004) Phase transition temperature ranges and storage density of paraffin wax phase change materials. *Energy* 29(11):1785–1804
- [10] Berardi U, Soudian S (2019) Experimental investigation of latent heat thermal energy storage using PCMs with different melting temperatures for building retrofit. *Energy Build* 185:180–195
- [11] Peng S, Fuchs A, Wirtz RA (2004) Polymeric phase change composites for thermal energy storage. *J Appl Polym Sci* 93:1240–1251
- [12] Dorigato A et al (2017) Polyethylene wax/EPDM blends as shape-stabilized phase change materials for thermal energy storage. *Rubber Chem Technol* 90(3):575–584
- [13] Bo H, Gustafsson EM, Setterwall F (1999) Phase transition temperature ranges and storage density of paraffin wax phase change materials. *Energy* 24(12):1015–1028
- [14] Lane GA (1983) *Solar heat storage: latent heat materials, vol II*. CRC Press, Boca Raton
- [15] Castellon C et al (2010) Effect of microencapsulated phase change material in sandwich panels. *Renew Energy* 5:2370–2374
- [16] Borreguero AM et al (2010) Improvement of the thermal behaviour of gypsum blocks by the incorporation of microcapsules containing PCMS obtained by suspension polymerization with an optimal core/coating mass ratio. *Appl Therm Eng* 30:1164–1169
- [17] Kuznik F et al (2011) A review on phase change materials integrated in building walls. *Renew Sustain Energy Rev* 15(1):379–391
- [18] Dorigato A, Fredi G, Pegoretti A (2019) Thermo-mechanical behavior of novel wood laminae-thermoplastic starch biodegradable composites with thermal energy storage/release capability. *Front Mater* 6:76
- [19] Sharma A et al (2009) Materials for advanced heat storage in buildings. *Renew Sustain Energy Rev* 13(2):318–345
- [20] Rigotti D, Dorigato A, Pegoretti A (2018) 3D printable thermoplastic polyurethane blends with thermal energy storage/release capabilities. *Mater Today Commun* 15:228–235

- [21] Dorigato A, Rigotti D, Pegoretti A (2018) Thermoplastic polyurethane blends with thermal energy storage/release capability. *Front Mater* 5:58
- [22] Fredi G et al (2018) Discontinuous carbon fiber/polyamide composites with microencapsulated paraffin for thermal energy storage. *J Appl Polym Sci* 136:47408
- [23] Fredi G, Dorigato A, Pegoretti A (2019) Novel reactive thermoplastic resin as a matrix for laminates containing phase change microcapsules. *Polym Compos* 40(9):3711–3724
- [24] Fallahi E, Barmad M, Haghghat KM (2010) Preparation of phase-change material microcapsules with paraffin or camel fat cores: application to fabrics. *Iran Polym J* 19(4):277–286
- [25] Salaün F et al (2010) Preparation and characteristics of n-nonadecane/cement composites as thermal energy storage materials in buildings. *Thermochim Acta* 506:82–93
- [26] Fredi G, Dorigato A, Pegoretti A (2018) Multifunctional glass fiber/polyamide composites with thermal energy storage/release capability. *eXPRESS Polym Lett* 12(4):49–364
- [27] Fredi G et al (2018) Multifunctional epoxy/carbon fiber laminates for thermal energy storage and release. *Compos Sci Technol* 158:101–111
- [28] European Parliament (2010) Directive 2010/31/EU of the European Parliament and of the Council of 19 May 2010 on the energy performance of buildings (recast)
- [29] Fredi G et al (2019) Docosane-organosilica microcapsules for structural composites with thermal energy storage/release capability. *Materials* 12(8):1286
- [30] Phadunghatthanakoon S, Poompradub S, Wanichwecharungruang SP (2011) Increasing the thermal storage capacity of a phase change material by encapsulation: preparation and application in natural rubber. *Appl Mater Interfaces* 3(9):3691–3969
- [31] Dorigato A et al (2017) Phase changing nanocomposites for low temperature thermal energy storage and release. *eXPRESS Polym Lett* 11(9):738–752
- [32] Fredi G et al (2017) Wax confinement with carbon nanotubes for phase changing epoxy blends. *Polymers* 9(9):405
- [33] Hong Y, Xin-shi G (2000) Preparation of polyethylene-paraffin compound as a form-stable solid-liquid phase change material. *Sol Energy Mater Sol Cells* 64(1):37–44
- [34] Krupa I, Mikova G, Luyt AS (2007) Polypropylene as a potential matrix for the creation of shape stabilized phase change materials. *Eur Polym J* 43(3):895–907
- [35] Sari A et al (2009) Poly(ethylene glycol)/poly(methyl methacrylate) blends as novel form-stable phase-change materials for thermal energy storage. *J Appl Polym Sci* 116(2):929–933
- [36] Cao Q, Pengsheng L (2006) Hyperbranched polyurethane as novel solid–solid phase change material for thermal energy storage. *Eur Polym J* 42(11):2931–2939
- [37] Kaygusuz K et al (2008) Encapsulated fatty acids in an acrylic resin as shape-stabilized phase change materials for latent heat thermal energy storage. *Energy Sources Part A Recov Utilization Environ Effects* 30:1050–1059
- [38] Xiao M, Feng B, Gong K (2002) Preparation and performance of shape stabilized phase change thermal storage materials with high thermal conductivity. *Energy Convers Manag* 43(1):103–108
- [39] Li R, Zhou Y, Duan X (2019) A novel composite phase change material with paraffin wax in tailings porous ceramics. *Appl Therm Eng* 151:115–123
- [40] Zhou X et al (2009) Preparation and thermal properties of paraffin/porous silica ceramic composite. *Compos Sci Technol* 69(7):1246–1249
- [41] Xiangfa Z et al (2010) Pore structure modification of silica matrix infiltrated with paraffin as phase change material. *Chem Eng Res Des* 88(8):1013–1017
- [42] Colombo P et al (2010) Polymer-derived ceramics: 40 years of research and innovation in advanced ceramics. *J Am Ceram Soc* 93(7):1805–1837
- [43] Vakifahmetoglu C, Zeydanli D, Colombo P (2016) Porous polymer derived ceramics. *Mater Sci Eng R Rep* 106:1–30
- [44] Sorarù GD et al (2012) Novel polysiloxane and polycarbosilane aerogels via hydrosilylation of preceramic polymers. *J Mater Chem* 22(16):7676
- [45] Jana P et al (2018) Polymer-derived SiCN cellular structures from replica of 3D printed lattices. *J Am Chem Soc* 101(7):2732–2738
- [46] Jana P, Zera E, Sorarù GD (2017) Processing of preceramic polymer to low density silicon carbide foam. *Mater Des* 116:278–286
- [47] Santhos B et al (2020) Processing and thermal characterization of polymer derived SiCN(O) and SiOC reticulated foams. *Ceram Int* 46(5):5594–5601
- [48] Brigo L et al (2018) 3D nanofabrication of SiOC ceramic structures. *Adv Sci* 5(12):1800937
- [49] Eckel ZC et al (2016) Additive manufacturing of polymer-derived ceramics. *Science* 351(6268):58–62
- [50] Zocca A et al (2013) SiOC ceramics with ordered porosity by 3D-printing of a preceramic polymer. *J Mater Res* 28(17):2243–2252
- [51] Kulkarni A, Sorarù GD, Pearce JM (2020) Polymer-derived SiOC replica of material extrusion-based 3-D printed plastics. *Addit Manuf* 32:100988
- [52] Dibandjo P et al (2005) Synthesis of boron nitride with ordered mesostructure. *Adv Mater* 17(5):571–574

- [53] Vakifahmetoglu C et al (2017) Gradient-hierarchical-aligned porosity SiOC ceramics. *Sci Rep* 7(1):41049
- [54] Yajima S, Hayashi J, Omori M (1975) Continuous silicon carbide fiber of high tensile strength. *Chem Lett* 4(9):931–934
- [55] Sorarù GD, Zera E, Jana P (2017) Processo per la produzione di corpi ceramici comprendenti nanofibre di nitruro o carburo di silicio e corpi ceramici così ottenuti, Domanda Italiana di Brevetto per Invenzione Industriale, N. 102017000133208 del 21 Novembre 2017
- [56] Biesuz M et al (2020) Polymer-derived Si₃N₄ nanofelts as a novel oil spills clean-up architecture. *J Environ Chem Eng* 8(5):104134
- [57] Biesuz M et al (2020) Polymer-derived Si₃N₄ nanofelts for flexible, high temperature, lightweight and easy-manufacturable super-thermal insulators. *Appl Mater Today* 20:100648
- [58] Widgeon SJ et al (2010) ²⁹Si and ¹³C Solid-state NMR spectroscopic study of nanometer-scale structure and mass fractal characteristics of amorphous polymer derived silicon oxycarbide ceramics. *Chem Mater* 22–23:6221–6228
- [59] Wen Q, Yu Z, Riedel R (2020) The fate and role of in situ formed carbon in polymer-derived ceramics. *Prog Mater Sci* 109:100623
- [60] Hirao K et al (2001) High thermal conductivity silicon nitride ceramic. *High Therm Conduct Mater* 26:451–455
- [61] Mehrali M et al (2013) Shape-stabilized phase change materials with high thermal conductivity based on paraffin/graphene oxide composite. *Energy Convers Manag* 67:275–282
- [62] Chen G et al (2020) An experimental and numerical investigation on a paraffin wax/graphene oxide/carbon nanotubes composite material for solar thermal storage applications. *Appl Energy* 264:114789
- [63] Zhang L et al (2016) Solar-thermal conversion and thermal energy storage of graphene foam-based composites. *Nanoscale* 8(30):14600–14607
- [64] Dong S et al (2017) Facile synthesis of silicon nitride nanowires with flexible mechanical properties and with diameters controlled by flow rate. *Sci Rep* 7(1):45538
- [65] Luongo JP (1983) Infrared characterization of α - and β -crystalline silicon nitride. *J Electrochem Soc* 130(7):1560–1563
- [66] Huang J et al (2012) Catalyst-assisted synthesis and growth mechanism of ultra-long single crystal α -Si₃N₄ nanobelts with strong violet–blue luminescent properties. *CrytEngComm* 14(21):7301–7305
- [67] Galvagnini F et al (2020) Multifunctional polyurethane foams with thermal energy storage/release capability. *J Therm Anal Calorim* (in press)
- [68] Qi G et al (2017) Hierarchical graphene foam-based phase change materials with enhanced thermal conductivity and shape stability for efficient solar-to-thermal energy conversion and storage. *Nano Res* 10(3):802–813
- [69] Lamvik M, Zhou JM (1995) Experimental study of thermal conductivity of solid and liquid phases at the phase transition. *Int J Thermophys* 16(2):567–576

Publisher's Note Springer Nature remains neutral with regard to jurisdictional claims in published maps and institutional affiliations.